TU Delft

Delft University of Technology

Document Version
Final published version

Licence
CC BY

Citation (APA)
Knoop, M. W., van Oudheusden, B. W., Pelkmans, L., & Schrijer, F. F. J. (2026). Passive transverse forcing of turbulent boundary-layer flow using sinusoidal surface grooves. *Experimental Thermal and Fluid Science*, *179*, Article 111842. https://doi.org/10.1016/j.expthermflusci.2026.111842

Important note
To cite this publication, please use the final published version (if applicable).
Please check the document version above.

Copyright
In case the licence states “Dutch Copyright Act (Article 25fa)”, this publication was made available Green Open Access via the TU Delft Institutional Repository pursuant to Dutch Copyright Act (Article 25fa, the Taverne amendment). This provision does not affect copyright ownership.
Unless copyright is transferred by contract or statute, it remains with the copyright holder.

Sharing and reuse
Other than for strictly personal use, it is not permitted to download, forward or distribute the text or part of it, without the consent of the author(s) and/or copyright holder(s), unless the work is under an open content license such as Creative Commons.

Takedown policy
Please contact us and provide details if you believe this document breaches copyrights.
We will remove access to the work immediately and investigate your claim.

This work is downloaded from Delft University of Technology.

Experimental Thermal and Fluid Science 179 (2026) 111842

Contents lists available at ScienceDirect

Experimental Thermal and Fluid Science

journal homepage: www.elsevier.com/locate/etfs

Passive transverse forcing of turbulent boundary-layer flow using sinusoidal surface grooves☆

Max W. Knoop *, Bas W. van Oudheusden, Luuk Pelkmans, Ferry F.J. Schrijer

Faculty of Aerospace Engineering, Delft University of Technology, Kluyverweg 1, Delft, 2628 HS, The Netherlands

ARTICLE INFO

Keywords:
Turbulent boundary layers
Drag reduction
Passive flow control
Theoretical modelling
Sinusoidal surface grooves
Stokes layer

ABSTRACT

A surface geometry consisting of parallel, meandering streamwise grooves has been experimentally studied as an alternative means of passive transverse forcing of turbulent boundary-layer flow. Particle image velocimetry (PIV) was the main diagnostic tool for characterising the properties of the induced spanwise flow. Contrary to the original expectation, the flow does not exhibit a spanwise-uniform undulation aligned with the grooves; instead, a converging-diverging flow pattern results. This flow pattern can be attributed to the spanwise periodicity of the lateral pressure gradient. The forcing effect is found to initially increase with the groove amplitude, but it saturates when the groove slope becomes too steep. The observed induced flow, referred to as a Passive Stokes Layer (PSL), can be considered as being composed of an inertial (pressure-driven) *outer solution* generated by the displacement effect of the non-smooth surface geometry, and a viscous *inner solution* to accommodate the no-slip condition at the wall. The mechanism of transverse flow generation is elucidated by an inviscid flow model that relates the forcing to the surface geometric properties, with predictions that are in good agreement with the experimental results. Although a reduction in the near-wall turbulence levels over the groove surfaces is observed, no direct evidence for drag reduction is apparent in the mean-flow data. Instead, an estimate of the frictional drag potential is based on establishing a tentative relation to an equivalent spatial Stokes layer (SSL) induced by active wall forcing. This theoretical comparison indicates that the induced passive forcing is sufficient to act on the (active) spanwise forcing mechanism, but produces at most a few per cent of frictional drag reduction. Any potential savings are likely offset by pressure drag and other losses, so that, similar to active forcing, its potential for net drag reduction in practical applications is limited.

1. Introduction

Flow control aimed at reducing turbulent skin-friction drag can lead to substantial energy savings, which may, for example, yield reduced carbon dioxide emissions in practical applications. A particularly effective strategy to achieve this type of drag reduction (DR) is the active and pre-determined imposition of a spatio-temporal wave of spanwise wall motion, for which high DR values of over 45% have been reported [for a review refer to 1]. This spanwise forcing induces a thin transverse-velocity shear layer – referred to as the Stokes layer [2] – that periodically interacts with the near-wall turbulence, driving the underlying DR mechanism [3–9]. While theoretical net-power savings of over 25% have been reported [10], in practice the overall power expenditure required to drive the spanwise flow in combination with losses in the entire actuation chain vastly outweighs these savings, by several orders of magnitude [refer to, e.g. 11–13]. In addition, these active control techniques are not easily adaptable to practical implementation in view of the system complexity associated with active forcing, which limits their adoption despite their promise of high DR and energy savings.

These considerations have motivated the study of passive control strategies that aim to induce a spanwise flow actuation similar to that induced by active methods. More specifically, the active analogue that such passive forcing methods aim to recreate is the steady spatially periodic forcing that imposes a spanwise wall velocity $w_w(x)$, according to

$$w_w(x) = W_{\mathrm{SSL}} \sin(k_x x), \tag{1}$$

where W_{SSL} is the spanwise velocity amplitude, and $k_x = 2\pi/\lambda_x$ indicates the streamwise wavenumber/wavelength. Throughout this paper, capital W is used to indicate the transverse velocity amplitude.

☆ This article is part of a Special issue entitled: 'FLUCOME 2025' published in Experimental Thermal and Fluid Science.

* Corresponding author.
E-mail address: m.w.knoop@tudelft.nl (M.W. Knoop).

https://doi.org/10.1016/j.expthermflusci.2026.111842
Received 1 June 2026; Received in revised form 23 July 2026; Accepted 9 September 2026
Available online 22 September 2026
0894-1777/© 2026 The Author(s). Published by Elsevier Inc. This is an open access article under the CC BY license (http://creativecommons.org/licenses/by/4.0/).

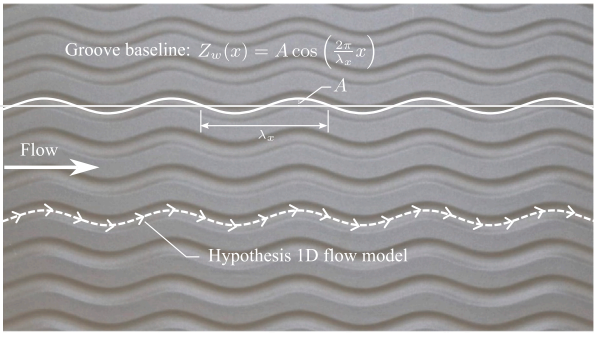


Fig. 1. Photograph of a SU test surface. Overlayed are the groove baseline definition and the hypothesised working principle (refer to Section 1.1).

Active forcing induces a so-called spatial Stokes layer (SSL), for which an analytical solution was formulated by Viotti et al. [14]. Instead of wall-based forcing, these passive control strategies produce a forcing of the bulk flow overlying the stationary wall. The efficacy of bulk-flow forcing is apparent from active strategies, based on, e.g. plasma actuators [15–17], acoustic excitation [18], and Lorentz force [19–21], that report similar DR to that of wall-based forcing.

In this study, we focus on passive strategies based on large-scale geometrical modifications of the surface, which include existing strategies such as oblique wavy walls [22,23] and shallow spherical dimples [24–27]. Both methods effectively generate an alternating cross-flow component by introducing a three-dimensional pressure gradient.

The present investigation addresses an alternative surface geometry described in a patent by Van Nesselrooij et al. [28], which is referred to as sinusoidal undulations (SU). A top-view of an SU test surface is shown in Fig. 1. The test-surface geometry constitutes shallow surface grooves that meander along the streamwise direction, with the proposed working principle that this will likewise induce an oscillatory spanwise component in the near-wall flow, in direct analogy to the active spatial (standing-wave) actuation referred to above. While SU may appear to resemble sinusoidal riblets, investigated for the same purpose of frictional DR [29–32], a key difference is their large-scale and shallow surface geometry versus the microscopic scale of riblets that make them sensitive to erosion and fouling in practice.

1.1. One-dimensional model for the transverse flow

A simplified prediction of the induced spanwise velocity is made by assuming that the flow is forced to follow the SU geometry perfectly. This hypothesis is visualised in Fig. 1. The SUs are described by a sinusoidal baseline

$$Z_w(x) = A\cos(k_x x) = A\cos\left(\frac{2\pi}{\lambda_x}x\right), \tag{2}$$

where x denotes the streamwise coordinate, A is the groove spanwise displacement amplitude, and k_x and λ_x are the streamwise wavenumber and wavelength analogous to the definitions for active forcing in Eq. (1). Assuming a constant convective velocity U_c provides a one-dimensional (1D) prediction of the spanwise velocity, as

$$w(x) = \frac{dZ_w}{dt} = \frac{dx}{dt}\frac{dZ_w}{dx} = -\underbrace{Ak_xU_c}_{W_{1D}}\sin(k_x x), \tag{3}$$

where W_{1D} is the predicted spanwise velocity amplitude. For turbulent boundary layers, the near-wall convection velocity is $U_c \approx 10U_\tau$ [33], where U_τ is the skin-friction velocity. Based on this, the 1D model predicts $W_{1D}/U_\tau \approx 3$ to 8 for the present SU geometries (refer to Table 2), which falls in the range of typical actively imposed velocity amplitudes of 2 to 12 U_τ.

This conceptual model is evidently a significant oversimplification of the real flow behaviour. Firstly, given the discrete groove arrangement, the flow is likely to exhibit spanwise variation rather than a spanwise-uniform deflection pattern. Moreover, the model does not take into account that the efficiency of the spanwise forcing is likely dependent on the groove cross-sectional geometry, if only for the reason that a zero groove depth will not result in any forcing. Hence, the forcing efficiency may be expected to increase with groove depth.

Later in this paper, we will consider a more realistic flow model that relates the lateral forcing mechanism to the groove geometry, providing a quantitative illustration and prediction of the flow forcing performance, and serving as a basis for comparison with experimental observations.

1.2. Research objectives

The research question this study aims to address is: *Can sinusoidal undulations induce effective passive forcing with potential for turbulent drag reduction?*

Five SU test geometries were investigated in a turbulent boundary layer (TBL) flow to establish the effect of varying groove amplitude A and cross-sectional geometry (details in Section 2.2). To characterise the flow over the test surfaces, particle image velocimetry measurements (details in Section 2.3) were conducted in the streamwise-wall-normal plane and in a near-wall wall-parallel plane. Results show that a passive type Stokes layer – referred to as the *passive Stokes layer* (PSL) – is induced by the test surfaces; its overall flow organisation for the mean flow and turbulence is established in Section 3. We elucidate the mechanism of spanwise flow generation in Section 4, supported by a potential-flow model that is detailed in Appendix A. The spanwise forcing characteristics of the PSL are quantified in Section 5 and compared with a predictive scaling derived from the SU geometric parameters using the potential-flow model. To draw an analogy with active spanwise wall-forcing, a three-dimensional (3D) viscous model of the PSL, derived in Appendix B, is used in Section 6 to compare with the active spatial Stokes layer (SSL) and to evaluate the performance; discussion on the DR potential is provided accordingly.

2. Methodology

2.1. Facility and test conditions

Experiments have been conducted in an open-return wind tunnel with a cross-sectional area of $0.4 \times 0.4\,\mathrm{m}^2$ and a typical free-stream turbulence intensity of 0.7%. Fig. 2(a) provides a schematic of the experimental setup for which the wind-tunnel configuration matches the experiments in [34]. The boundary-layer flow was generated on a 30-mm thick flat plate with an elliptic leading edge and tripped to turbulence by a strip of 24-grit sand-grain roughness. A canonical flat-plate TBL subsequently developed over a streamwise extent of 3 m, after which the test surfaces under investigation were mounted flush with the wall of the incoming TBL.

The streamwise, wall-normal, and spanwise coordinates are denoted by (x, y, z), and the corresponding instantaneous velocity components are (u, v, w); p denotes pressure. Instantaneous quantities are decomposed into a mean and fluctuating part as denoted by an overbar and prime superscript, e.g. $u = \overline{u} + u'$. The y coordinate starts at the top face of the SU geometry (the flat wall regions in between the grooves). As indicated in Fig. 2, the origin of the coordinate system is located at the upstream edge of the PIV field-of-view, which is 2.44 m downstream of the TBL trip.

Viscous scaling, indicated by the superscript '+', is adopted using the kinematic viscosity ν and the skin-friction velocity U_τ. The characteristic viscous length-scale is defined by $\delta_\nu = \nu/U_\tau$. All viscous scaling is based on U_τ of the corresponding flat-plate (i.e., smooth-surface) TBL flow, in order to reveal absolute changes relative to a common

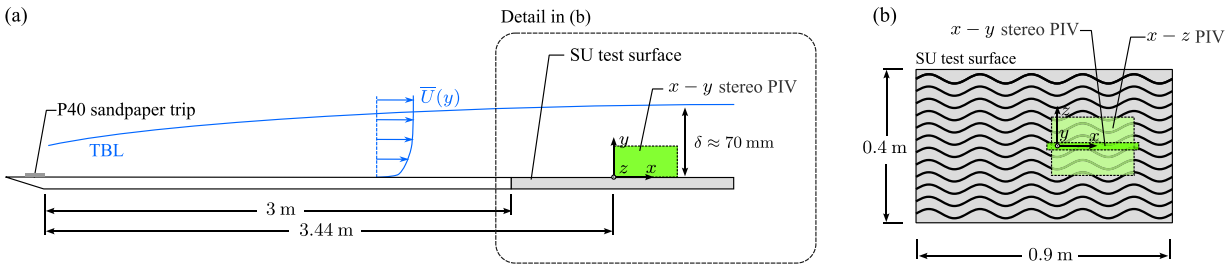


Fig. 2. (a) Schematic of wind-tunnel configuration and (b) detail of the particle image velocimetry (PIV) experiments over the SU test-surface.

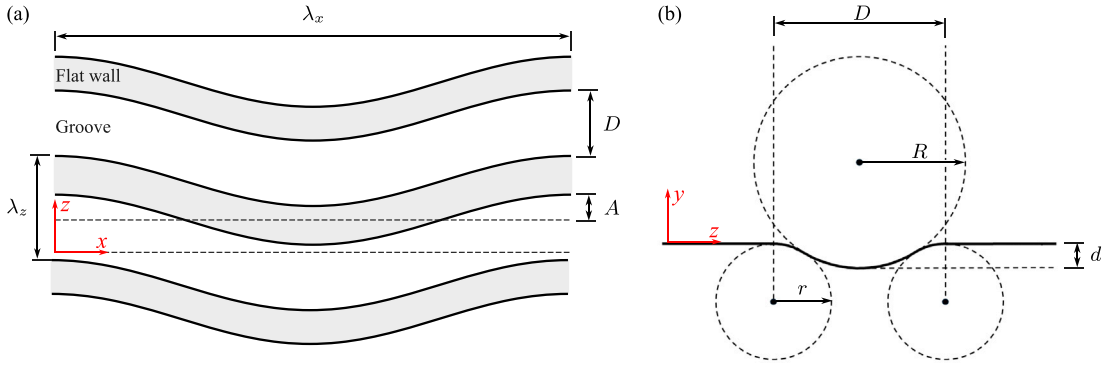


Fig. 3. Schematic of the SU geometry, (a) top-view, (b) groove cross-section.

Table 1
Overview of the free-stream conditions, boundary layer characteristics, and viscous scaling parameters based on a reference flat-plate TBL flow.

U_∞ (m/s)	δ (mm)	U_τ (m/s)	δ_ν (μm)	Re_τ
5	70	0.217	68.9	1020
7.5	69	0.308	48.6	1410

reference. U_τ and a wall-normal offset correction to account for any deviations from the initial determination of the wall-position [35], were determined by fitting the mean streamwise velocity to a composite velocity profile by Chauhan et al. [36] using the log-layer parameters $\kappa = 0.384$ and $B = 4.17$. As the present measurements do not cover the full boundary-layer height, the boundary layer thickness δ was taken from a previous TBL characterisation using hot-wire anemometry (employing the same composite fitting procedure). Table 1 shows the experimental conditions and viscous scaling parameters based on the flat-plate reference surface. Experiments were carried out for free-stream velocities of $U_\infty = 5$ and 7.5 m/s, with corresponding $Re_\tau = \delta U_\tau/\nu$ of 1020 and 1410.

2.2. Test surfaces

A flat-plate reference surface and five SU models are considered. Each aluminium test surface was CNC-machined and measures $881 \times 366\,\text{mm}^2$ in the streamwise and spanwise direction. The bare aluminium surfaces had machining marks of very small dimensions of less than 0.01 mm, which is equivalent to $0.2\delta_\nu$ at $U_\infty = 7.5$ m/s. Nevertheless, to provide a consistent surface finish across all test surfaces, they were wrapped with a vinyl sticker.

The SU geometry, schematically shown in top-view in Fig. 3(a), consists of parallel grooves that follow the sinusoidal baseline along the streamwise direction, as defined in Eq. (2), with wavelength λ_x and spanwise displacement amplitude A. The spacing of adjacent grooves is given by its spanwise wavelength λ_z. Fig. 3(b) displays the cross-sectional groove profile that is derived from the dimple geometry in [26] and is defined by its width D and depth d, with an edge rounding radius $r = D$.

Table 2
Geometrical parameters of the SU test surfaces. The left side reports the dimensional values in mm, and the right side reports the appropriate scaling of the parameters.

Model ID	Dimensional (mm)					Scaled			
	A	D	d	λ_x	λ_z	α_{max} (°)	A/λ_x	d/D	λ_z/D
A3-D10-d050	3.24	10	0.5	57.18	16.5	19.6	0.057	0.050	1.65
A5-D10-d050	5.25	10	0.5	57.18	16.5	30.0	0.092	0.050	1.65
A7-D10-d050	7.64	10	0.5	57.18	16.5	40.0	0.134	0.050	1.65
A3-D10-d025	3.24	10	0.25	57.18	16.5	19.6	0.057	0.025	1.65
A3-D20-d100	3.24	20	1	57.18	33	19.6	0.057	0.050	1.65

Table 3
Viscous scaled geometric parameters of the SU test surfaces.

Model ID	$U_\infty = 5$ m/s					$U_\infty = 7.5$ m/s				
	A^+	D^+	d^+	λ_x^+	λ_z^+	A^+	D^+	d^+	λ_x^+	λ_z^+
A3-D10-d050	47.9	145	7.3	830	240	66.7	206	10.3	1180	340
A5-D10-d050	76.2	145	7.3	830	240	108.1	206	10.3	1180	340
A7-D10-d050	110.9	145	7.3	830	240	157.3	206	10.3	1180	340
A3-D10-d025	47.9	145	3.6	830	240	66.7	206	5.1	1180	340
A3-D20-d100	47.9	290	14.5	830	479	66.7	412	20.6	1180	680

Table 2 presents an overview of the five test-surface geometries considered to assess the effect of groove amplitude and cross-sectional shape. Model A3-D10-d050 serves as a baseline geometry, designed in analogy to the staggered dimple configuration 'plate A' in van Nesselrooij et al. [26] by setting λ_x and λ_z to the streamwise and spanwise dimple spacing and matching d/D. Our results show that the groove baseline is appropriately scaled by A/λ_x while the spanwise cross-section is appropriately scaled using D, i.e. d/D and λ_z/D. The maximum slope of the grooves, which occurs at $x/\lambda_x = 0.25, 0.75$, provides an indicator of the spanwise velocity amplitude, based on the 1D model (refer to Section 1.1), and is given by

$$\alpha_{max} = \tan^{-1}(Ak_x). \tag{4}$$

Table 4
Uncertainty quantification of the PIV statistics based on the flat-plate TBL.

	$U_\infty = 5$ m/s			$U_\infty = 7.5$ m/s		
	$\epsilon^+_{\overline{u}}$	$\epsilon^+_{\overline{w}}$	$\epsilon^+_{\overline{u'u'}}$	$\epsilon^+_{\overline{u}}$	$\epsilon^+_{\overline{w}}$	$\epsilon^+_{\overline{u'u'}}$
$x-z$ PIV	0.059	0.027	0.0069	0.037	0.019	0.0027
$x-y$ S-PIV	0.077	0.057	0.012	0.051	0.039	0.0053

The viscous scaled geometric parameters are presented in Table 3, which shows that the streamwise wavelength is close to $\lambda_x = 1000$ where optimum DR for active forcing occurs [9,14].

2.3. Particle image velocimetry

Particle image velocimetry (PIV) experiments were conducted in two different plane orientations, as shown in Fig. 2(b). Either one or two digital LaVision sCMOS cameras (2160 × 2560 pixels, 16-bit, 6.5 μm pixel size) were used for image acquisition, an Evergreen Nd:YAG (532 nm) 200 mJ/pulse laser was used for illumination, and 1 μm water-glycol droplets were used for seeding.

Planar two-velocity component (2D-2C) measurements were conducted in a wall-parallel $x-z$ plane with a field-of-view of 92×78 mm^2. A single sCMOS camera was used with a 105-mm focal-length lens at aperture $f/5.6$. The laser sheet was centred at $y \approx 1$ mm, with a $\Delta y_s \approx 1.4$ mm thickness, i.e. the illumination covered a region of $y_s \approx 1 \pm 0.7$ mm. In viscous units, this corresponds to a laser sheet located at $y_s^+ \approx 15 \pm 10$ and 21 ± 14 for $U_\infty = 5.0$ and 7.5 m/s, respectively. 2000 two-pulse snapshots were acquired at 15 Hz, with a time separation of $\Delta t = 150$ and 100 μs between image pairs for the two respective free-stream velocities. To remove background laser-sheet reflections in the raw images, each image was divided by the time-average over all images. Velocity vectors were computed using a multi-pass (3 passes) cross-correlation algorithm with an iterative window deformation method [37,38]. The final pass used Gaussian-weighted interrogation windows (IWs) of 48 × 48 pixels, at an overlap factor of 75%; this choice resulted in a viscous-scaled spatial resolution (i.e. IW size) of approximately $25 \times 25\ \delta_v^2$ and $35 \times 35\ \delta_v^2$, respectively.

In addition, stereoscopic-PIV (2D-3C) measurements were conducted in the streamwise-wall-normal x–y plane aligned along the undulation centreline. The field-of-view spanned 67 × 52 mm^2, with a laser-sheet thickness of $\Delta z_s \approx 1.3$ mm. For these measurements, two cameras were used with the same 105 mm focal length and an aperture of $f/16$. The cameras were calibrated using a pinhole model with a LaVision type-7 calibration plate (5-mm marker spacing). Ensembles of 1000 two-pulse snapshots were acquired at 6 Hz and with $\Delta t = 105$ and 75 μs. The same image pre-processing procedure as for the planar measurements was adopted. To enhance the wall-normal resolution, Gaussian-weighted rectangular IWs with a 4:1 aspect ratio were used for the vector calculations. The final IW size was 48 × 12 pixels at 75% overlap, resulting in a viscous spatial resolution of approximately $25 \times 6\ \delta_v^2$ and $35 \times 9\ \delta_v^2$.

The statistical uncertainty of the PIV measurements is quantified following Sciacchitano and Wieneke [39]. For a quantity χ, the uncertainty ϵ of the mean and variance are given by

$$\epsilon_{\overline{\chi}} = \sqrt{\frac{\overline{\chi'\chi'}}{N}} \quad \text{and} \quad \epsilon_{\overline{\chi'\chi'}} = \overline{\chi'\chi'}\sqrt{\frac{2}{N-2}}, \tag{5}$$

where N is the ensemble size, i.e. the number of uncorrelated PIV snapshots. Table 4 presents the viscous-scaled uncertainty of the mean flow components $\overline{u}$ and $\overline{w}$, as well as the streamwise velocity variance $\overline{u'u'}$, on the basis of the highest variance observed for the reference flat-plate TBL flow.

3. Overall flow organisation

Model A3-D10-d050 is considered as the baseline geometry in the current results discussion, for which the mean flow is characterised in the near-wall wall-parallel plane (Section 3.1) and in the streamwise-wall-normal plane (Section 3.2). The effect of the SU test surfaces on the near-wall turbulence is described in Section 3.3. All presented results correspond to the measurements at $U_\infty = 5$ m/s and $Re_\tau = 1020$ (details in Table 1), unless stated otherwise.

3.1. Near-surface wall-parallel mean flow

The wall-parallel flow organisation, located at the the wall-normal height of the laser sheet $y_s^+ \approx 15 \pm 10$, is characterised in Fig. 4 in terms of the streamwise (Fig. 4a) and spanwise (Fig. 4b) velocity component fields. Spanwise $\overline{w}$ profiles at $x/\lambda_x = 0.25$ and 0.75, which correspond to the locations where the groove slope is steepest (i.e. $\alpha_{\max}$ in Eq. (4)), are shown in Fig. 4(c). In this top-view of the flow, the transparent grey shading indicates the flat wall regions between the grooves, whereas the grooves are unshaded (similar as in Fig. 3a).

The streamwise flow (Fig. 4a) is modulated by the surface, with regions of high and low streamwise velocity that coincide, respectively, with the grooves ($\overline{u}^+ \approx 9$) and the flat wall between them ($\overline{u}^+ \approx 6.5$). Since the grooves lie below the top face of the test surface, measurements over the grooves are located farther from the surface within the overlying boundary layer, and consequently, the velocity is higher there. These results appear to confirm that the near-wall boundary layer follows the surface geometry and remains predominantly attached.

The spanwise velocity in Fig. 4(b) follows the grooves and qualitatively exhibits the hypothesised behaviour based on the 1D model in Section 1.1. Namely, the strongest transverse flow within the groove is induced where the groove slope dZ_w/dx is steep and thus scales in proportion to and matches the sign of $w(x)$ in Eq. (3). The primary flow regions that follow the grooves alternate spanwise with patterns of opposing sign in the regions between the grooves (transparent grey shading). This feature was not predicted by the 1D model and indicates a secondary flow directed across the groove edges rather than along its axis. The primary and secondary flows are driven by a spanwise-periodic pressure gradient induced by the groove geometry; its mechanism is further elucidated in Section 4.

The primary flow produces the maximum spanwise velocity of $\overline{w}^+ \approx \pm 0.4$, which occurs right downstream of the maximum groove slope at $x/\lambda_x = 0.3$ and 0.8. Based on the profiles in Fig. 4(c), the secondary flow has a lower magnitude with double peaks. These peaks align with the groove edges, and the largest of the two secondary peaks occurs where the directions of the primary and secondary flows diverge.

Fig. 5 shows the effect of increasing the groove amplitude A on the spanwise flow, where $A/\lambda_x = 0.06$ corresponds to the results discussed above. As the amplitude increases from $A/\lambda_x = 0.06$ to 0.09 in Fig. 5(a) and (b), the $\overline{w}$ magnitude increases as may be expected based on a proportional scaling according to the 1D model (refer to Eq. (3)). This effect, however, is observed to saturate for the largest amplitude in Fig. 5(c) and does not mark a further increase in spanwise velocity. For $A/\lambda_x = 0.13$ it appears that the groove meandering is too strong to effectively contain the near-wall flow, which instead spills over the sides of the grooves.

3.2. Streamwise-wall-normal mean flow

Fig. 6 shows the mean flow in a streamwise-wall-normal plane along the centreline of the groove, i.e. $z = 0$. The wall is indicated by the grey patch. To account for the height variation of the test surfaces, a local wall-normal distance $\hat{y}$ is introduced that is measured from the actual surface. Note that for $x/\lambda_x < 0.6$, near-wall data below $\hat{y}^+ \approx 5$ were removed due to limited optical access to and laser-sheet reflections on the inside of the groove.

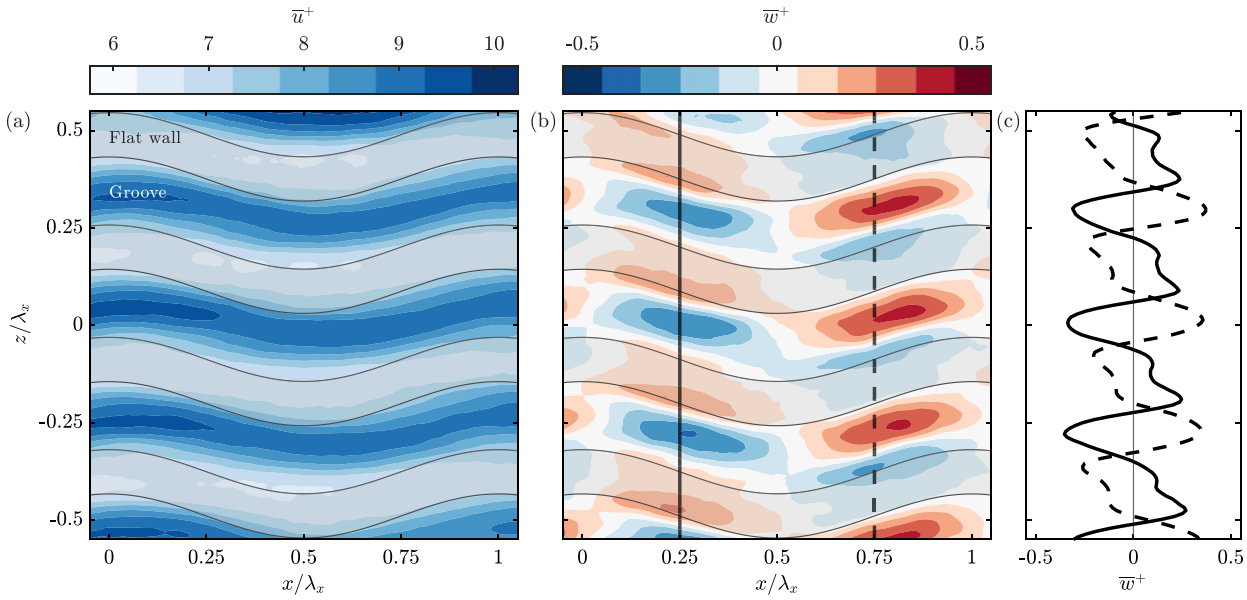


Fig. 4. Mean flow in the wall-parallel plane at $y_s^+ \approx 15 \pm 10$ for SU model A3-D10-d050 at $Re_\tau = 1020$. (a) Streamwise velocity $\overline{u}^+$, (b) spanwise velocity $\overline{w}^+$, and (c) spanwise $\overline{w}^+$ profiles located at $x/\lambda_x = [0.25, 0.75]$ as indicated by the vertical lines in (b) with the same linestyle. Grey-shaded regions represent the flat wall between grooves; grooves are unshaded.

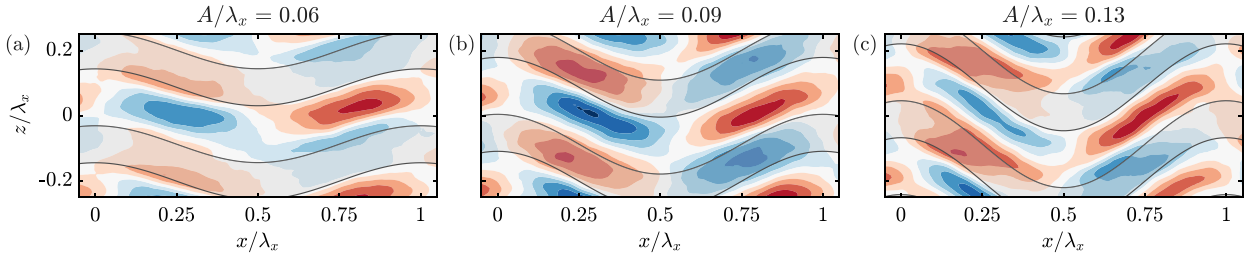


Fig. 5. Effect of increasing groove amplitude A on $\overline{w}^+$ in the wall-parallel plane for SU models (a) A3-D10-d050, (b) A5-D10-d050, and (c) A7-D10-d050. Colour scales are the same as in Fig. 4.

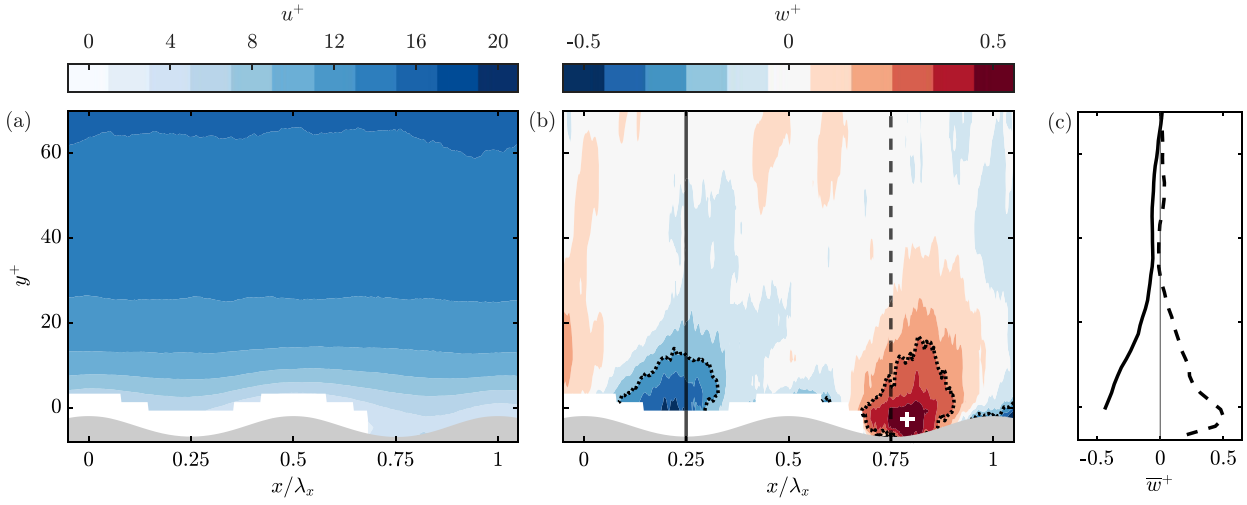


Fig. 6. Mean flow in the streamwise-wall-normal plane along the centreline of a groove for SU model A3-D10-d050 at $Re_\tau = 1020$. (a) Streamwise velocity $\overline{u}^+$, (b) spanwise velocity $\overline{w}^+$, and (c) wall-normal $\overline{w}^+$ profiles located at $x/\lambda_x = [0.25, 0.75]$ as indicated by the vertical lines in (b) with the same linestyle. The grey region represents the SU surface.

Fig. 6(a) shows that the $\overline{u}$ isolines deflect towards the surface for $y^+ < 20$. No reverse streamwise flow occurs, confirming that the flow remains attached to these shallow surface grooves (note that the data aspect ratio in the figure is approximately 10:1 in x:y). For the spanwise flow in Fig. 6(b), a streamwise-periodic alternating flow appears that shows resemblance to the characteristics of the active spatial Stokes

layer (SSL) in Viotti et al. [14]. We refer to this shear layer as the *passive Stokes layer* (PSL).

There are however key differences between the SSL and the PSL. In the active SSL situation, the spanwise velocity amplitude W_{SSL} is imposed at the wall, whereas here the spanwise flow is constrained to $\overline{w} = 0$ at the surface in view of the no-slip condition. Consequently, the PSL is bulk-driven by the 3D pressure gradient induced by the surface, such that W_{max} occurs away from the wall. The profiles in Fig. 6(c) show that a type of *two-region shear layer* forms with an inflexion around the location of W_{max}, similar to that of a wall jet [40]. A thin, viscous inner layer forms, which is most alike the SSL, while the outer layer exhibits a more gradual wall-normal decay, which is characterised by an outer penetration depth Δ.

We find that for the considered case, $W^+_{max} = 0.69$ is located at $\hat{y}^+ \approx 6$ away from the surface, indicated by the white-plus marker in Fig. 6(b). This height is similar to the inner-layer penetration depth for the SSL at equivalent λ_x of $\delta^+_s = 5.03$ (refer to Eq. (B.7)). To determine the penetration depth of the outer layer, we take the contour where $|\overline{w}|$ decays to $W_{max}e^{-1}$, as shown by the black-dotted isoline in Fig. 6(b), and select the highest y-location to be Δ, defined as

$$\Delta := \max\left\{ y \;\middle|\; \overline{w}(x,y) = W_{max}e^{-1} \right\}. \tag{6}$$

In Fig. 6(b), $\Delta^+ \approx 20$, which is indeed much thicker than the viscous inner layer. This deeper outer layer is caused by the gradual wall-normal decay of the near-wall pressure gradients induced by the surface, and is of inertial rather than viscous nature. Assuming that in the outer region of the PSL $\overline{w}$ follows approximately an exponential decay, $\overline{w}(y) = W_{max}\exp(-y/\Delta)$, a theoretical estimate of the uncertainty ϵ_Δ of Δ can be related to the velocity measurement uncertainty $\epsilon_{\overline{w}}$, as

$$\epsilon_\Delta = \frac{\epsilon_{\overline{w}}}{\partial\overline{w}/\partial y(y=\Delta)} = e\frac{\Delta}{W_{max}}\epsilon_{\overline{w}}, \tag{7}$$

which yields a relative uncertainty of Δ of approximately 23 and 15%, at $U_\infty = 5$ and 7.5 m/s, respectively. In practice, we find, based on the height variation of the contour lines, that a more realistic estimate is $\epsilon_{\Delta^+} \approx 2$, or approximately 10%.

3.3. Effects on turbulence

For the three groove amplitudes depicted in Fig. 5, wall-normal profiles of the mean streamwise velocity $\langle\overline{u}\rangle_x$, and the streamwise normal Reynolds stress $\langle\overline{u'u'}\rangle_x$ are shown in Fig. 7. The $\langle\ldots\rangle_x$ operator denotes streamwise averaging of the statistics across $0 \le x \le \lambda_x$, which serves to evaluate the integral effect. Measurements over the flat-plate reference surface are also included. Recall that scaling is based on U_τ of the flat-plate TBL, in order to appreciate the absolute changes in the statistics.

The inner peak in streamwise normal stress distribution in Fig. 7(b) reflects the high energetic content of the near-wall high- and low-speed velocity streaks that are central to the self-sustaining near-wall cycle [41,42]. Compared with the flat-plate reference (in black), the SU test surfaces exhibit a substantial reduction in the inner peak at $y^+ = 15$. For the two lower amplitudes $A/\lambda_x = 0.06$ and 0.09, the reduction of the inner-peak is similar, even though the latter produces a higher $\overline{w}$ magnitude in the wall-parallel plane (refer to Fig. 5). The strongest effect is produced by the large-amplitude surface $A/\lambda_x = 0.13$ that shows a 13% reduction relative to the flat-plate reference. Fig. 7(c) displays additionally the turbulence kinetic energy (TKE), which is obtained by summing all normal stress components. This profile reflects a similar trend as that for $\langle\overline{u'u'}\rangle_x$, indicating that the overall near-wall energy in the TBL is reduced, rather than redistributed over the different components.

While these results appear to suggest that the near-wall streaks are suppressed to some extent, the mean streamwise velocity Fig. 7(a) does not exhibit discernible differences from the flat-plate TBL or signs of a drag-reduced flow, such as the near-wall ($y^+ < 20$) momentum deficit that occurs in the case of DR by active spanwise forcing.

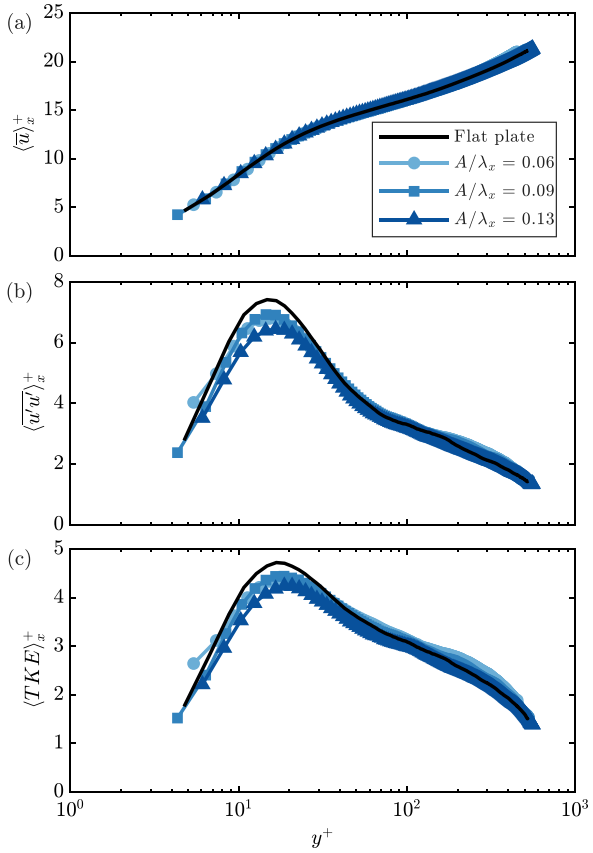


Fig. 7. Wall-normal turbulence statistics profiles for increasing groove amplitude at $Re_\tau = 1020$. (a) Streamwise velocity $\langle\overline{u}\rangle^+_x$, (b) streamwise normal stress $\langle\overline{u'u'}\rangle^+_x$, and (c) turbulence kinetic energy defined by $TKE = 0.5(\overline{u'u'} + \overline{v'v'} + \overline{w'w'})$.

4. Mechanisms of transverse flow generation

The mechanism of transverse flow generation is elucidated by supporting the measurements with a theoretical flow model. In this model, the flow is described as a uniform streamwise base flow that is perturbed by the groove geometry. Similar to Prandtl's original boundary-layer concept, and in line with the observations made in Section 3.2, we may consider the flow disturbance as composed of an inertial (pressure-driven) *'outer solution'* that is generated by the displacement effect of the non-smooth surface geometry, and a viscous *'inner solution'* to accommodate the no-slip condition at the wall, which generates a near-wall spatial Stokes layer. The outer solution is modelled as a (steady, inviscid, and incompressible) potential flow that is subject to the flow-tangency condition at the wall. In case of a sufficient scale separation, this outer solution provides a good representation of the characteristics of the forcing, such as the maximum transverse velocity and the penetration height. The potential-flow model is described in detail in Appendix A, and relevant results will be referenced in the main text discussion where appropriate. It is emphasised that the theoretical model presented herein is not intended as a highly accurate description of the flow, but instead as a conceptual model to explain the first-order trends observed in the experiments. Comparison of the model results with the actual experimental data will serve to further evaluate the approximate first-order (linearised) description.

Fig. 8(a,b) compare $\overline{w}$ in the wall-parallel plane of the measurements and the potential-flow model (refer to Eq. (A.20)). The potential flow model is evaluated at the same wall-normal height as the PIV measurement plane. For the measurements in Fig. 8(a), the streamlines

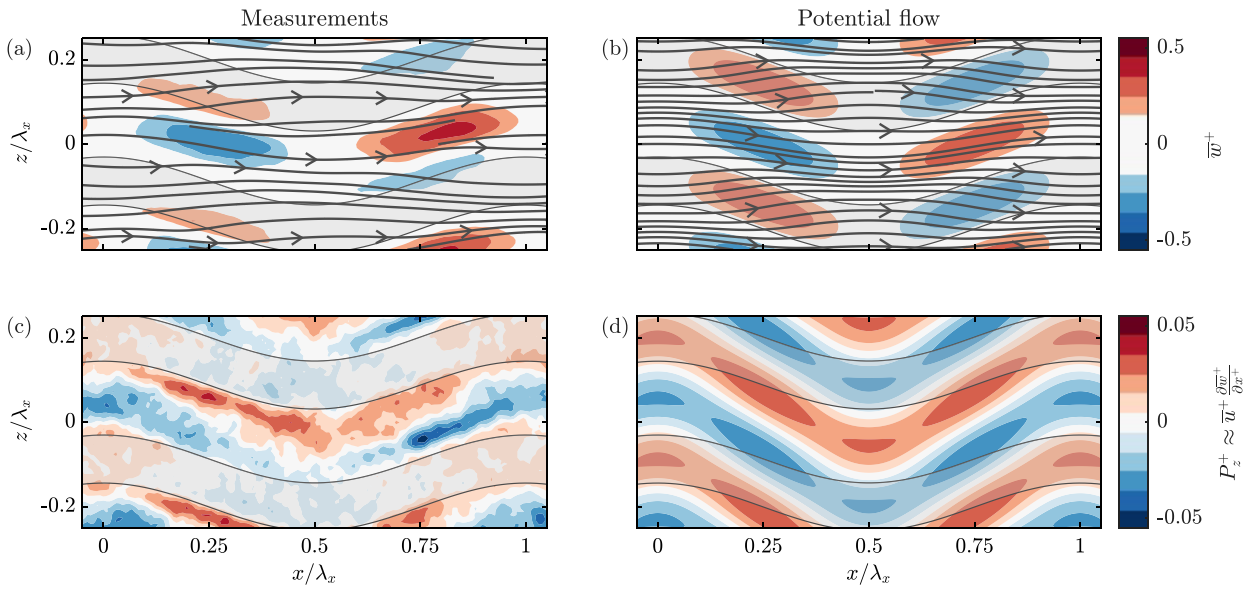


Fig. 8. Comparison of wall-parallel flow for (a,c) measurements over A3-D10-d050 and (b,d) potential flow computed at the laser-sheet height $y_s = 1$ mm. (a,b) Mean spanwise velocity $\overline{w}^+$ and streamlines for which spanwise velocity is $5\overline{w}$ to support interpretability. (c,d) Streamwise advection term $\overline{u}^+(\partial\overline{w}^+/\partial x^+)$ that is the leading order spanwise pressure gradient term.

within the groove show that the flow is deflected to align with the groove orientation, producing the primary flow structure established based on the 1D model in Section 3.1. Instead, near the groove edges around $x/\lambda_x = 0.25, 0.75$, a converging-diverging flow pattern appears, which causes the secondary flow on the flat wall between the grooves. This converging-diverging flow is centred around the locations of maximum spanwise displacement of the grooves, i.e. $x/\lambda_x = 0, 0.5, 1$. Upstream of the location at $x/\lambda_x = 0.5$, the flow is seen to enter the groove across its edge and converges, followed downstream by a diverging flow exiting the groove. The same converging-diverging flow has been observed for dimples [26], which is understandable in view of the similarity between the local shape of the groove and the dimple geometry.

Fig. 8(b) shows that potential flow provides a good prediction of the primary and secondary flow regions. In the potential-flow model, the magnitudes of the primary and secondary flows are equal owing to the sinusoidal spanwise groove profile assumed (refer to Appendix A), i.e. the flat wall between grooves is represented by a sinusoidal ridge. The converging-diverging flow topology is also well predicted. These results provide confidence that potential flow can be used for first-order predictions of the flow over shallow surface deformations. Moreover, the good agreement between the model predictions and the experimental data demonstrates that the passive bulk-flow forcing is essentially an inertial mechanism, with viscous effects playing only a secondary role.

Spanwise flow generation is ultimately driven through a bulk-forcing by the spanwise pressure gradient force P_z induced by the SU test surface, which is governed by the spanwise momentum balance

$$P_z = -\frac{1}{\rho}\frac{\partial \overline{p}}{\partial z} = \overline{u}_i\frac{\partial \overline{w}}{\partial x_i} + \frac{\partial \overline{w'u_i'}}{\partial x_i} - \nu\frac{\partial^2 \overline{w}}{\partial x_i^2}, \tag{8}$$

where ρ is the fluid density (i is the free index that denotes summing over the three coordinate directions). An order of magnitude analysis, based on both experimental data and the potential-flow model, reveals that the inertial streamwise advection term constitutes the leading-order contribution, such that

$$P_z \approx \overline{u}\frac{\partial \overline{w}}{\partial x}. \tag{9}$$

Fig. 8(c,d) compare the measurements with potential flow for this leading-order term. Despite noise in the measurements due to the spatial gradient computation, the overall organisation of $\overline{u}\partial\overline{w}/\partial x$ shows good correspondence with the potential-flow counterpart.

The discussion regarding the working mechanism of the spanwise forcing is supported by a conceptual sketch in Fig. 9. Along the span, the maxima and minima in P_z align with the centre of the grooves at $x/\lambda_x = 0, 0.5, 1$, i.e. the locations of the maximum lateral displacement of the groove baseline. As a result, a streamwise altering pressure-gradient force pattern is established that *'guides'* the flow along the groove axis. The spanwise variation of the P_z iso-lines is larger than the spanwise displacement of the groove A, so that along the groove the P_z sign alternates, from negative at $x/\lambda_x = 0$ to positive at $x/\lambda_x = 0.5$, and so on. Consequently, a pressure gradient near $x/\lambda_x = 0.25,\ 0.75$ between the grooves opposes that of the upstream primary P_z inside the grooves, which drives the secondary flow and ultimately results in the observed diverging-converging flow topology.

5. Quantification of spanwise-forcing characteristics

The spanwise forcing effect is assessed by characterising the passive Stokes layer (PSL) induced by the SU test surfaces, in terms of maximum spanwise velocity amplitude $W_{\max}$ and the outer-layer penetration depth Δ. In Section 5.1, the geometric scaling of these properties is first presented using the potential-flow model of Appendix A and subsequently compared to the experimental results in Section 5.2.

5.1. Geometric scaling based on potential-flow model

The geometric scaling of $W_{\max}$ in terms of the SU geometric parameters follows from the potential-flow model according to Eq. (A.20), as

$$W_{\text{pot}} = Adk_xk_zU_c. \tag{10}$$

As a first observation, we can derive from this expression a forcing efficiency with respect to the idealised 1D model, Eq. (3), to be

$$\frac{W_{\text{pot}}}{W_{\text{1D}}} = dk_z = 2\pi\frac{d}{\lambda_z} = 2\pi\frac{D}{\lambda_z}\frac{d}{D}. \tag{11}$$

Here, the groove width D has been introduced as a convenient characteristic spanwise length scale to replace the spanwise wavelength λ_z; these parameters are in fixed proportion for all test surfaces considered

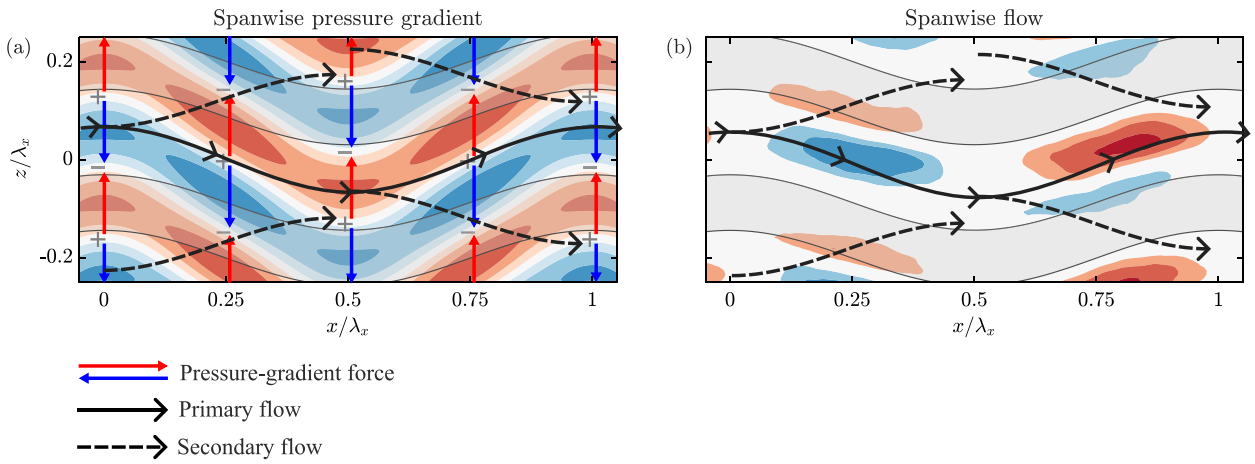


Fig. 9. Conceptual sketch for the mechanism of spanwise flow generation. (a) Spanwise pressure gradient, where grey '+' and '−' indicate high- and low-pressure regions and red/blue arrows show the resultant pressure-gradient force. (b) mean spanwise flow induced by the SU test surface. Overlayed lines show the primary flow (solid) and secondary flow (dashed) generated.

($\lambda_z/D = 1.65$, refer to Table 2). Eq. (11) shows that the forcing efficiency is predicted to be proportional to the depth-to-width ratio of the groove, and for the test surfaces with $d/D = 0.05$ this yields a theoretical forcing efficiency of 19% as compared to $W^+_{1D} \approx 3-8$, which is in excellent agreement with the present observations.

The scaling for the maximum spanwise velocity, Eq. (10), can be rewritten as

$$\frac{W_{pot}}{U_c} = Adk_xk_z = c\frac{A}{\lambda_x}\frac{d}{D}, \tag{12}$$

where c is a constant given by

$$c = 2\pi k_z D = 4\pi^2 \frac{D}{\lambda_z} \approx 24. \tag{13}$$

Eq. (12) predicts that the spanwise flow is (i) proportional to the convection velocity U_c, (ii) increases with increasing groove amplitude, where A/λ_x determines the maximum groove slope and can be considered as the *'groove-baseline aspect ratio'*, and (iii) increases (decreases) for deeper (shallower) groove depths, where d/D can be considered as the *'groove-profile aspect ratio'*.

Similarly, the scaling of the outer-layer penetration depth Δ follows from the potential-flow model, Eq. (A.16), as

$$\frac{\Delta}{D} = \frac{1}{Dk_z} = \frac{\lambda_z}{2\pi D} \approx 0.26. \tag{14}$$

This reveals that Δ is predicted to follow a geometrical scaling and, to first order (i.e. within the approximations underlying the potential-flow model), to scale directly proportional to the groove width D, without further influence of the other dimensional characteristics, such as the groove depth (d), groove amplitude (A) and the groove streamwise length scale (λ_x).

5.2. Passive Stokes layer characteristics

Fig. 10 displays the spanwise-forcing characteristics for all five test surfaces and for both free-stream velocities at $U_\infty = 5$ and 7.5 m/s ($Re_\tau = 1020$ and 1410), shown in red (solid lines) and blue (dotted lines), respectively. These characteristics are computed from the PIV data as outlined in Section 3.2. The scaling of the horizontal axis follows the suggestion of the potential-flow model, as discussed in Section 5.1. Model A3-D10-d050 is considered as the baseline geometry, with $A/\lambda_x = 0.06$, $d/D = 0.05$ (5%) and $D = 10$ mm. The other test surfaces varied only one geometric parameter at a time: increasing groove amplitude in circle markers, decreasing groove depth to $d/D = 0.025$ (2.5%) in square markers, and scaling the self-similar groove geometry by a factor of two to $D = 20$ mm in triangular markers. For further details, see Tables 2 and 3.

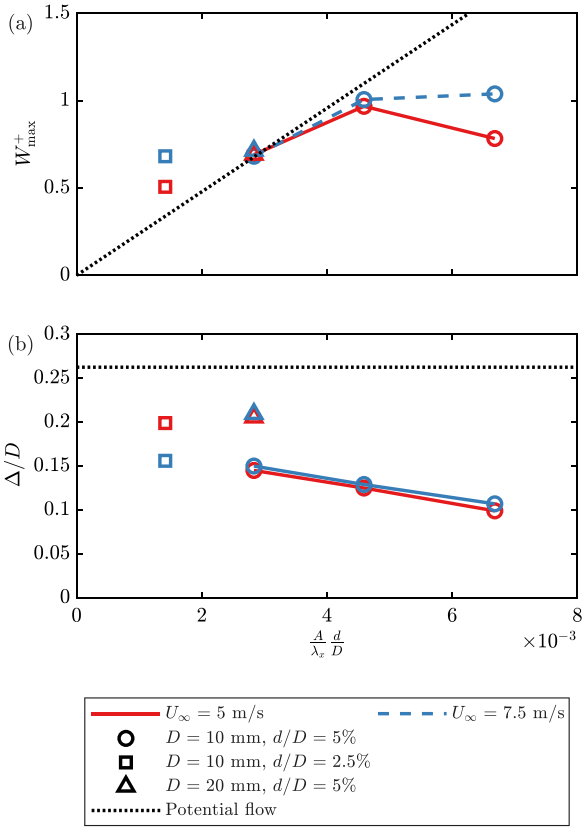


Fig. 10. Quantification of the spanwise forcing parameters based on all measurements. (a) Maximum spanwise velocity W^+_{max} and (b) outer-layer penetration depth Δ/D. Black dotted line gives potential flow estimates (a) $W_{pot} = Adk_xk_zU_c$ for $U_c^+ = 10$, and (b) $\Delta = 1/k_z$.

As the groove amplitude A increases (circle markers), W_{max} in Fig. 10(a) initially increases, in good agreement with the potential-flow scaling (dotted line), after which it levels and departs from the linear scaling for the largest amplitude. This trend is consistent with the flow organisation in Fig. 5. For the intermediate amplitude, W^+_{max} is lower than the potential-flow prediction, indicating the departure from the

linearised assumption on which the model relies as the surface slope becomes steeper. The correct scaling of the velocity amplitude with $\frac{A}{\lambda_x}\frac{d}{D}$ is confirmed by the upscaled but self-similar groove (triangle markers), which exhibits the same $W_{\max}$ as the baseline groove (circle markers). The shallower grooves (square markers) show a reduction in $W_{\max}$ of about half, and although the spread is large owing to experimental uncertainty, this trend aligns with the predicted theoretical scaling. No strong influence of the free-stream velocity is observed as long as $\frac{A}{\lambda_x}\frac{d}{D}$ remains below 4.5×10^{-3}, confirming that the convection velocity in W_{pot} and $W_{\max}$ scales proportionally with U_τ (or U_∞, the influence of Re_τ is small and these velocity scales are essentially linearly dependent). The highest velocity amplitude induced by the SU models is $W^+_{\max}=1$ at $A/\lambda_x=0.09$ ($\frac{A}{\lambda_x}\frac{d}{D}=4.5\times10^{-3}$), which amounts to approximately 5% of U_∞.

The potential-flow scaling breaks down when $\frac{A}{\lambda_x}\frac{d}{D}\gtrsim 4.5\times10^{-3}$ (note that according to Eq. (A.14), the surface gradient $\max(\partial h/\partial x)$ follows the same scaling as this quantity), where the surface slope further increases and flow separation may occur. In this regime, the influence of U_∞ is also apparent, indicating that the flow is indeed more complex and cannot be reliably predicted with a linearised potential-flow model. Based on these results, a criterion $\frac{A}{\lambda_x}\frac{d}{D}\lesssim 4.5\times10^{-3}$, or equivalent $Adk_xk_z\lesssim 0.1$, is proposed as the limit on the maximum surface slope for the SU geometry. Despite these quantitative discrepancies when the flow-response becomes non-linear, the potential-flow model provides a useful and novel tool to predict the first-order effects of small surface height variations.

Fig. 10(b) shows the variation of Δ/D, the outer-layer penetration depth normalised by the groove width. The experimental data appear to conform to a geometrical scaling of Δ, but with deviations from the theoretical prediction of a constant value Δ/D, although the order of magnitude agrees. A linearly decreasing trend between Δ/D and $\frac{A}{\lambda_x}\frac{d}{D}$ is observed for the experimental data. This trend does not break down for increasing A/λ_x (circled markers), so it seems that the outer layer, produced by wall-normal decay of near-surface perturbations, is less susceptible to steep surface curvature than the value of $W_{\max}$. Its proportionality to D is more complex; namely, the upscaled self-similar groove (triangle markers) has a higher Δ/D than the baseline model (circle markers). We can, however, confirm that the variation in Δ/D with respect to the model does not impact the prediction of $W_{\max}$ in view of the agreement between model and experiment in Fig. 10(a).

6. Discussion on drag reduction by passive forcing

So far, we have considered only the inertial outer-layer solution for the passive Stokes layer (PSL), based on the potential-flow model, which enabled us to quantitatively relate the induced flow characteristics to the surface geometry. In this section, we use an analytical model of the full PSL solution that includes viscous effects, providing the complete inner-outer-layer structure established in Section 3.2. The derivation is given in Appendix B. We first compare the PSL to the active SSL and experimental results in Section 6.1. To provide insight into the potential of the lateral flow forcing of the PSL, in Section 6.2, we match the forcing amplitude $W_{\max}$ to that of an equivalent SSL amplitude W_{eq} (based on equivalence of the surface-averaged Stokes strain), so as to compare to the DR results in Viotti et al. [14].

6.1. Analytical model for the passive Stokes layer

A comparison between the experiments and theory is made for the baseline model A3-D10-d050 at $Re_\tau=1020$, using the characteristics $W_{\max}$ and Δ (given in Fig. 10) as input for the PSL model. The first and second columns of Fig. 11 show the SSL and PSL analytical solutions at $z=0$. In the third column, the two models are compared using wall-normal profiles, for which the experimental $\overline{w}$ profiles (Fig. 6c) are included as well. The top row shows the spanwise velocity $\overline{w}$, and the bottom row shows the Stokes strain $\partial\overline{w}/\partial y$.

In Fig. 11(a), the classic SSL solution is depicted, which is dominated by viscous effects as characterised by its near-wall ($y^+<15$), forward-inclined shear layer that is driven by the wall velocity. Instead, the PSL in Fig. 11(b) conforms to the two-region structure introduced in Section 3.2, characterised by a viscous inner layer below $y^+<10$ to satisfy the no-slip condition, and an inertial (pressure-driven) outer layer that extends to a much higher wall-normal distance of $y^+\approx 60$. Qualitatively, the $\overline{w}$ contours of the PSL match the experimental results in Fig. 6(b), which is further supported by the comparison of the wall-normal profiles in Fig. 11(c). There are some quantitative differences, for example, in the precise streamwise locations where $W_{\max}$ occurs and in the slightly stronger outer-layer solution of the analytical model. However, given the approximations underlying the theoretical model (refer to Appendix B), the quantitative discrepancies are of secondary importance. The key result is the strong qualitative agreement between the PSL model and the experiment, which lends mutual support to the proposed flow organisation.

6.2. Analogy with active forcing and drag reduction potential

In view of the essential differences in flow structure between the bulk-forced PSL and the actively wall-driven SSL, the velocity amplitude $W_{\max}$ of the PSL does not directly compare to that of the SSL, which prevents a one-on-one comparison to the DR(W_{SSL}) relation established in Viotti et al. [14]. To overcome this discrepancy, $W_{\max}$ is mapped onto an equivalent active forcing amplitude W_{eq}, by matching the Stokes strain of the two models, similar to the approach taken in Ghebali et al. [23] for oblique wavy walls. The Stokes strain is an appropriate choice for this procedure, since it, or derived measures, provides an effective diagnostic of DR [43–46], and it has been proven relevant to the physical DR mechanism [6–9]. We consider the surface-averaged Stokes strain magnitude at the wall, computed as

$$S=\frac{1}{\lambda_x\lambda_z}\int_0^{\lambda_z}\int_0^{\lambda_x}\frac{\partial|w|(\hat{y}=0)}{\partial y}\,dx\,dz. \tag{15}$$

S is first computed for both models at unit amplitude, indicated by their respective subscripts. W_{eq} is then related to $W_{\max}$ according to

$$W_{\mathrm{eq}}=\frac{S_{\mathrm{PSL}}}{S_{\mathrm{SSL}}}W_{\max}. \tag{16}$$

The two models in Fig. 11 are matched based on S, such that $W^+_{\max}=0.69$ (as observed in the experiment) corresponds to an effective amplitude of $W^+_{\mathrm{eq}}=0.54$. This lower effective amplitude is in part attributed to the spanwise-periodic PSL solution compared to the spanwise-uniform SSL solution, which would, theoretically, be a factor $2/\pi\approx0.63$ lower given the average value of $|\cos(k_z z)|$. Consequently, the local near-wall Stokes strain in Fig. 11(d–f) is higher in the case of the PSL. In practice, we find that the ratio is approximately 0.8, i.e. $W_{\mathrm{eq}}\approx 0.8W_{\max}$, indicating that the PSL is less effective than the SSL at the same velocity amplitude.

Applying the same matching procedure for the strongest passive forcing case at $W^+_{\max}=0.97$ (refer to Fig. 10), yields $W^+_{\mathrm{eq}}=0.78$. To compare $W^+_{\mathrm{eq}}=0.78$ to the DR reported in Viotti et al. [14], we extrapolate their results at $\lambda_x=1250$ at $Re_\tau=200$ (these are effectively linear for their $W^+_{\mathrm{SSL}}=[1,2,6]$), for which we find an approximate frictional DR of 1.8%. This result suggests that the PSL produces sufficient Stokes strain to act on the spanwise-forcing drag-reduction mechanisms. Nevertheless, this small theoretical estimate is likely degraded by an unfavourable Re_τ scaling [47] and added pressure drag due to the surface geometry.

To place this frictional DR estimate in context, a 1 to 3% skin-friction DR was reported for oblique wavy walls by Ghebali et al. [23]. However, this saving was largely offset by pressure drag, leading to either a small total DR of up to 0.7% or an overall drag increase. A similar conclusion was drawn for dimples by Van Campenhout et al. [27]. Using numerical simulations, they found a total drag increase of

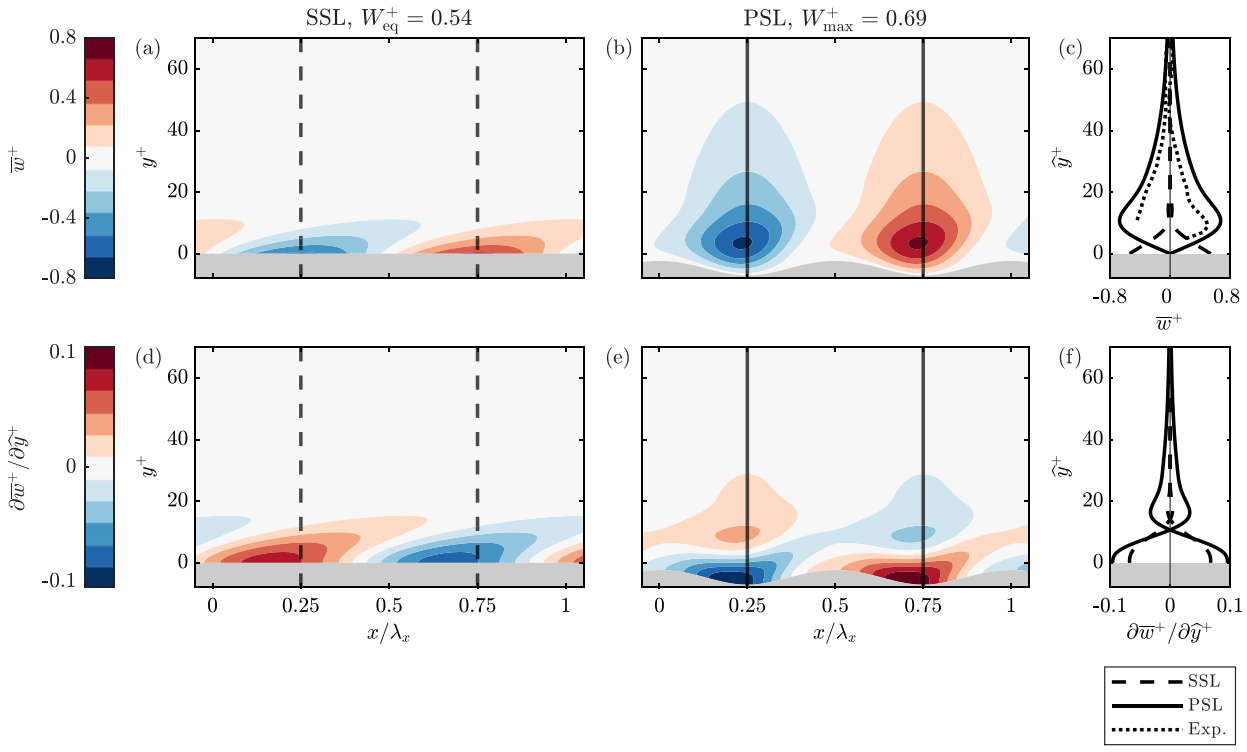


Fig. 11. Comparison of the active spatial Stokes layer (SSL) and passive Stokes layer (PSL) for model A3-D10-d050. The first and second columns show streamwise-wall-normal contours for (a,d) the SSL, (b,e) the PSL; the third column (c,f) compares the wall-normal profiles at $x/\lambda_x = [0.25, 0.75]$. The top and bottom row show (a–c) mean spanwise velocity, and (d–f) wall-normal Stokes strain $\partial\overline{w}^+/\partial\widehat{y}^+$.

1 to 2%, whereas the experiments by van Nesselrooij et al. [26] initially reported a 4% DR.

While a rigorous experimental characterisation of the total drag for all SU test surfaces is outside the scope of the present study, preliminary direct-force drag measurements of model A3-D10-d050 were conducted by Knoop [48]. These results are mentioned here, not to draw quantitative conclusions, but rather to provide an impression in support of this discussion of the DR potential. The measurements employed the direct force balance and methodology of Van Nesselrooij et al. [49], which improved on that of van Nesselrooij et al. [26], and were validated for dimples and riblets in [27]. For SU model A3-D10-d050, as well as several other passive test surfaces, these measurements reported no change in total drag relative to a flat-plate reference within a ±0.5% uncertainty interval.

All these results suggest that, in line with earlier results on dimples and oblique wavy walls, the investigated SU geometry may produce a small amount of turbulent skin-friction DR, however, this saving is likely offset by an increase in pressure drag, yielding a few per cent of net DR at most. Any remaining DR potential will further degrade when implemented in industrial applications (e.g. Re_τ-scaling and limited coverage), making it unlikely that passive spanwise forcing for turbulent DR will be practically relevant.

7. Summary and conclusions

Parallel sinusoidal surface grooves, meandering along the streamwise direction, and referred to as sinusoidal undulations (SU), were explored for their potential to passively generate transverse forcing, motivated by the high DR achievable via active spanwise forcing. Particle image velocimetry (PIV) in combination with analytical modelling was used to characterise the flow over five SU test surfaces, to elucidate the mechanisms of spanwise flow generation and the formation of the passive Stokes layer, and to support a discussion of its DR potential.

Results show that the SU test surfaces are effective at generating a streamwise-alternating transversal flow. A primary flow is directed along the grooves, which is alternated in the spanwise direction by a secondary flow in the opposing direction, producing a flow out of the groove across its edges; combined, the primary and secondary flow creates a converging-diverging flow pattern.

The mechanism of transverse flow generation was elucidated using a potential flow model based on the surface geometry. The surface displacement and the flow tangency condition cause a spanwise pressure gradient that drives an inertial bulk-flow forcing and produces an exponentially decaying outer-layer. The outer-layer solution obtained by the potential-flow model provides excellent first-order predictions of the experimental results. Near the surface, viscous effects dominate, forming a thin inner layer to accommodate the no-slip condition. The combined inner-outer solution forms the *passive Stokes layer* (PSL), for which an analytical solution is derived based on the pressure-gradient forced advection-diffusion equation of the spanwise momentum.

The potential-flow solution provided a theoretical estimate of the maximum spanwise velocity amplitude and its scaling with respect to the surface geometry. When the spanwise cross-section remains self-similar (i.e. constant d/D and D/λ_z), the predicted amplitude scales as: $W_{pot} \propto U_c \frac{A}{\lambda_x}\frac{d}{D}$, hence, being proportional to (i) the convection velocity (taken as $U_c = 10U_\tau$), (ii) A/λ_x signifying the aspect ratio between groove spanwise displacement and streamwise wavelength, and (iii) the relative groove depth d/D. Experimental results confirm the validity of scaling the PSL characteristics using $\frac{A}{\lambda_x}\frac{d}{D}$, showing an excellent quantitative prediction of $W^+_{max} = 0.69$ for the baseline SU test-surface. Further confirmation of this scaling is provided by an upscaled but self-similar geometry (i.e. the same $\frac{A}{\lambda_x}\frac{d}{D} = 2.8 \times 10^{-3}$) that exhibits the same measured W_{max} as the baseline. The effect of increasing groove amplitude A/λ_x is initially an expected increase in velocity amplitude, up to a maximum of $W^+_{max} \approx 1$, after which the velocity amplitude saturates and departs from the theoretical trend. This deviation is likely owing to the linearised boundary condition of the model and possible flow separation when the surface inclination becomes too steep. We find that the theoretical scaling is appropriate

when $\frac{A}{\lambda_x}\frac{d}{D} \lesssim 4.5 \times 10^{-3}$ or equivalently $Adk_xk_z \lesssim 0.1$. The efficiency of the spanwise flow generation, compared to an initial assumption that the flow follows the groove perfectly, translating the streamwise velocity into a spanwise component, is approximately 20% for both experiment and the theoretical prediction, and is found to depend on the spanwise cross-section dk_z (related to d/D).

The viscous inner-layer of the PSL is representative of the spatial Stokes layer (SSL) as induced by active spanwise forcing. Quantitatively matching the surface-averaged Stokes strain of the SSL and PSL analytical solutions shows that $W_{\max}$ of the PSL is equivalent to approximately 80% of the active wall-velocity amplitude, i.e. $W_{\text{eq}} \approx 0.8W_{\max}$. This theoretical comparison suggests that SU geometry is effective at inducing a modest Stokes strain to act upon the established spanwise-forcing mechanism for skin-friction DR. While the real physics of how the PSL affects the flow turbulence may be more complex, this exercise provides an indication of its performance relative to the established DR characteristics of its active counterpart. Extrapolating the results of Viotti et al. [14] suggests an approximate 1.8% reduction of frictional drag. These potential savings, however, are likely offset by additional pressure drag and other inefficiencies in practice. So, while some degree of frictional DR may be achieved with passive forcing, its potential as an alternative means to active spanwise forcing in practical applications appears to remain limited.

CRediT authorship contribution statement

Max W. Knoop: Writing – review & editing, Writing – original draft, Supervision, Methodology, Investigation, Formal analysis, Conceptualization. **Bas W. van Oudheusden:** Writing – review & editing, Writing – original draft, Methodology, Conceptualization. **Luuk Pelkmans:** Writing – review & editing, Methodology, Investigation, Formal analysis. **Ferry F.J. Schrijer:** Methodology, Conceptualization.

Declaration of competing interest

The authors declare that they have no known competing financial interests or personal relationships that could have appeared to influence the work reported in this paper.

Acknowledgements

The authors gratefully acknowledge the financial support of the Netherlands Enterprise Agency (RVO) under grant number TSH21002. We are sincerely thankful to the team at Dimple Aerospace B.V., namely, Michiel van Nesselrooij, Olaf W. G. van Campenhout, and Friso H. Hartog, for their close collaboration and years of extensive research into passive flow control strategies aimed at turbulent skin-friction drag reduction.

Appendix A. Potential-flow model based on the surface geometry

As discussed in the main text (Section 4), a model for transverse flow actuation by SU surface grooves is proposed, based on a potential flow approach. For the convenience of the analysis, the surface geometry of streamwise aligned surface grooves is approximated by a spanwise sinusoidal groove profile, which gives a parametric description of the surface height

$$h(x,z) = -d\cos(k_z\hat{z}), \quad \text{where} \quad \hat{z} = z - A\cos(k_x x). \tag{A.1}$$

Here A, d, k_x and k_z correspond to the geometric parameters introduced in Section 2.2.

The velocity vector $\mathbf{u} = (u, v, w)$ is expressed as the gradient of the velocity potential ϕ:

$$\mathbf{u} = \nabla\phi. \tag{A.2}$$

The potential is decomposed into a streamwise-uniform flow at convection velocity U_c and a small perturbation φ induced by the surface geometry, as

$$\phi(x,y,z) = U_c x + \varphi(x,y,z), \tag{A.3}$$

The (perturbation) potential needs to satisfy the Laplace equation (mass conservation), i.e

$$\nabla^2\phi = \nabla^2\varphi = 0. \tag{A.4}$$

with boundary conditions:

$$\varphi(x,\infty,0) = 0, \tag{A.5}$$

$$\nabla\phi(x,0,z)\cdot\mathbf{n} = 0, \tag{A.6}$$

where $\mathbf{n}$ is the surface normal vector given by

$$\mathbf{n} = \left(-\frac{\partial h}{\partial x}, 1, -\frac{\partial h}{\partial z}\right). \tag{A.7}$$

The conditions expressed in (A.5) and (A.6) correspond to, respectively, a decay of the perturbation as $y \to \infty$ and flow-tangency at the surface.

Using separation of variables, the solution of φ is sought in the form

$$\varphi = g(x,z)\,f(y), \tag{A.8}$$

Evaluating the Laplace equation, we find

$$\frac{f_{yy}}{f} = -\frac{g_{xx}+g_{zz}}{g} = \text{constant} \tag{A.9}$$

where the subscripts denote partial differentiation with respect to the given variable. Eq. (A.9) is constant (defined below) as a consequence of the variable separation. Solving the left-hand side for f, with normalisation $f(0) = 1$, yields

$$f(y) = e^{-y/\Delta}, \tag{A.10}$$

which reveals an exponential decay of the velocity perturbation, i.e. $f(\infty) = 0$, that satisfies the boundary condition in (A.5). The exponential decay length, Δ, introduced here is similar to the wall-normal penetration depth as defined in Section 3.2. This result furthermore identifies the value of the constant in Eq. (A.9) as being equal to $1/\Delta^2$.

The second boundary condition in (A.6), the flow-tangency condition at the surface, is linearised around $y = 0$; neglecting the higher-order terms gives

$$\frac{\partial\varphi(x,0,z)}{\partial y} = U_c\frac{\partial h(x,z)}{\partial x}. \tag{A.11}$$

Substituting Eqs. (A.8) and (A.10) then yields

$$g(x,z) = -U_c\Delta\frac{\partial h(x,z)}{\partial x}, \tag{A.12}$$

The estimate of the penetration depth Δ is provided by evaluating the right-hand side of (A.9). Here, the streamwise gradient term g_{xx} is neglected w.r.t. g_{zz}, since the characteristic spanwise length scale is much smaller than the streamwise one, i.e. $\lambda_x \gg \lambda_z$. With this approximation, we find

$$\frac{1}{\Delta^2} \approx -\frac{g_{zz}}{g} = -\frac{h_{xzz}}{h_x}, \tag{A.13}$$

where

$$h_x = \frac{\partial h(x,z)}{\partial x} = dAk_xk_z\sin(k_x x)\sin(k_x\hat{z}), \tag{A.14}$$

and

$$h_{xzz} = \frac{\partial^3 h(x,z)}{\partial x\partial z^2} = -dAk_xk_z^3\sin(k_x x)\sin(k_x\hat{z}) \tag{A.15}$$

which gives

$$\Delta = \frac{1}{k_z}. \tag{A.16}$$

Collecting all results, the perturbation potential can be expressed as

$$\varphi(x,y,z) = -U_c\Delta\frac{\partial h(x,z)}{\partial x}e^{-y/\Delta} = -U_c A d k_x \sin(k_x x)\sin(k_z\hat{z})e^{-y/\Delta}. \tag{A.17}$$

Solving for the velocity components yields

$$u(x,y,z) = U_c + \frac{\partial\varphi}{\partial x} \approx U_c, \tag{A.18}$$

$$v(x,y,z) = \frac{\partial\varphi}{\partial y} = U_c A d k_x k_z \sin(k_x x)\sin(k_z\hat{z})e^{-y/\Delta} \tag{A.19}$$

and

$$w(x,y,z) = \frac{\partial\varphi}{\partial z} = -\underbrace{U_c A d k_x k_z}_{W_{\text{pot}}}\sin(k_x x)\cos(k_z\hat{z})e^{-y/\Delta}. \tag{A.20}$$

W_{pot} provides the maximum spanwise velocity at $y = 0$, which serves as a first-order estimate of the maximum spanwise velocity induced by the surface grooves.

Appendix B. Three-dimensional model of the passive Stokes layer

To complement the potential flow model derived in Appendix A, which represents the outer layer of the passive Stokes layer (PSL), this Appendix considers a viscous flow model for the entire PSL by including a viscous term in order to satisfy the no-slip condition at the wall. The analysis follows the same (laminar flow) approach, which Viotti et al. [14] applied to the active spatial Stokes layer (SSL). Here, the PSL is considered as a perturbation of a parallel base flow $(u(y), 0, 0)$. When further assuming that the thickness of the PSL is small with respect to the streamwise wavelength, the (linearised) spanwise-momentum equation reads

$$u\frac{\partial w}{\partial x} = \underbrace{-\frac{1}{\rho}\frac{\partial p}{\partial z}}_{P_z} + \nu\frac{\partial^2 w}{\partial y^2}, \tag{B.1}$$

subject to the boundary conditions $w(x,0,z) = w(x,\infty,z) = 0$. In (B.1) P_z represents the spanwise pressure-gradient force, similar to that in Eq. (8).

When further assuming a linear streamwise velocity profile, the governing equation becomes

$$(u_0 y)\frac{\partial w}{\partial x} - \nu\frac{\partial^2 w}{\partial y^2} = P_z, \tag{B.2}$$

where u_0 is the wall-normal gradient of the streamwise velocity at the surface, i.e. $(\partial u/\partial y)_{y=0} = U_\tau^2/\nu = U_\tau/\delta_\nu$. This result is identical to the governing equation for the SSL, as considered by Viotti et al. [14], apart from the additional forcing term P_z. The SSL solution, hence, provides the homogeneous solution of (B.2), and the total solution can therefore be expressed as a combination with a particular solution arising from the pressure-gradient forcing.

We first simplify the three-dimensional solution into a planar solution, using the coordinate transformation $\hat{z} = z - A\cos(k_z x)$ (introduced in (A.1)) that represents the spanwise location relative to the groove baseline, and by defining $w(x,y,z) = \widetilde{w}(x,y)\cos(k_z\hat{z})$. Introducing these transformations in (B.2) and dividing out the term $\cos(k_z\hat{z})$ yields the spanwise momentum equation for $\widetilde{w}(x,y)$,

$$u_0 y\frac{\partial\widetilde{w}}{\partial x} - \nu\frac{\partial^2\widetilde{w}}{\partial y^2} = \widetilde{P}_z. \tag{B.3}$$

In view of (B.3), an estimate of the magnitude of $\widetilde{P}_z$ is based on the consideration that in the outer layer the pressure gradient is balanced by the inertia term, such that

$$\widetilde{P}_z \sim -(u_0 y)\frac{\partial\widetilde{w}_o}{\partial x}. \tag{B.4}$$

where $\widetilde{w}_o$ refers to the outer solution, as represented by Eq. (A.20). This leads to the following model for the spanwise pressure gradient:

$$\widetilde{P}_z = -(u_0 y)P_0\cos(k_x x)e^{-y/\Delta}, \tag{B.5}$$

where P_0 is a constant, given by $P_0 = A d k_x^2 k_z U_c$ according to the potential-flow model. For the current purpose, however, P_0 is treated as a constant of which the value can be tuned to produce a desired value of the velocity amplitude $W_{\max}$.

By introducing $\widetilde{w}(x,y) = \Re[e^{ik_x x}E(y)]$ ($\Re$ denotes the real part) into (B.3), an ordinary differential equation is obtained:

$$i\delta_s^{-3} y E - E_{yy} = -\frac{u_0 P_0}{\nu}\, y\, e^{-y/\Delta}, \tag{B.6}$$

with the Stokes layer thickness defined as

$$\delta_s = \left(\frac{\nu}{u_0 k_x}\right)^{1/3}. \tag{B.7}$$

Introducing the change of variable

$$y = e^{-i\pi/6}\delta_s\xi, \quad \text{and} \quad F(\xi) = E(e^{-i\pi/6}\delta_s\xi), \tag{B.8}$$

rotates the wall-normal coordinate into the decaying sector of the Airy equation and transforms the homogeneous problem into its canonical form, as given in [14]. This choice ensures that the physically admissible solution is given by the decaying Airy function of the first kind, i.e. $\mathrm{Ai}(\xi) \to 0$ as $\xi \to \infty$. The governing equation then becomes

$$F_{\xi\xi} - \xi F = \underbrace{Q\xi e^{-\xi/\Delta_\xi}}_{f(\xi)}, \tag{B.9}$$

with

$$Q = -\frac{iP_0}{k_x}, \quad \text{and} \quad \Delta_\xi = \frac{\Delta}{e^{-i\pi/6}\delta_s}. \tag{B.10}$$

The left-hand side of (B.9) corresponds to the Airy equation with linear operator $\mathcal{L} = (\mathrm{d}/\mathrm{d}\xi)^2 - \xi$ that is forced by $f(\xi)$ on the right-hand side. The solution for $F(\xi)$ is sought in the form of its homogeneous and particular solution,

$$F(\xi) = F_h(\xi) + F_p(\xi). \tag{B.11}$$

The homogeneous equation admits two linearly independent solutions given by the Airy functions of the first and second kind, $\mathrm{Ai}(\xi)$ and $\mathrm{Bi}(\xi)$. Since $\mathrm{Ai}(\xi)$ is the only function that decays exponentially as $\xi \to \infty$, while $\mathrm{Bi}(\xi \to \infty)$ grows without bound, the solution to the homogeneous equation is $F_h(\xi) = \gamma\mathrm{Ai}(\xi)$. The full solution is then written as

$$F(\xi) = \gamma\mathrm{Ai}(\xi) + F_p(\xi), \tag{B.12}$$

where the constant γ is determined from the no-slip boundary condition $\widetilde{w}(x,0) = 0$ (equivalently $F(0) = 0$) and found to be

$$\gamma = -\frac{F_p(0)}{\mathrm{Ai}(0)}. \tag{B.13}$$

Green's function is used to obtain the particular solution. To this end, the two fundamental solutions $\mathrm{Bi}(\xi)$ and $\mathrm{Ai}(\xi)$ are chosen such that the first one satisfies the boundary condition at the wall, i.e. $\mathrm{Bi}(0) \neq 0$ to ensure $\gamma \neq 0$, and the second one satisfies decay in the far field, i.e. $\mathrm{Ai}(\xi \to \infty) = 0$. The Green's function associated with the operator $\mathcal{L}$ of (B.9) and satisfying decay in the far field is given by [50]

$$G(\xi,s) = \frac{1}{W}\begin{cases}\mathrm{Bi}(s)\mathrm{Ai}(\xi), & s < \xi,\\ \mathrm{Bi}(\xi)\mathrm{Ai}(s), & s > \xi,\end{cases} \tag{B.14}$$

where the Wronskian of the fundamental two solutions is constant and given by

$$W = \mathrm{Bi}(\xi)\mathrm{Ai}'(\xi) - \mathrm{Bi}'(\xi)\mathrm{Ai}(\xi) = \frac{1}{\pi}. \tag{B.15}$$

The particular solution is then obtained using the convolution of the Green's function $G(\xi, s)$ with the forcing term:

$$F_p(\xi) = \int_0^\infty G(\xi,s)f(s)ds = \pi Q \mathrm{Ai}(\xi)\int_0^\xi \mathrm{Bi}(s)s\, e^{-s/\Delta_\xi} ds + \pi Q \mathrm{Bi}(\xi)\int_\xi^\infty \mathrm{Ai}(s)s\, e^{-s/\Delta_\xi} ds. \tag{B.16}$$

Collecting all results, the analytical solution for the PSL is given by

$$w(x,y,z) = \cos(k_z\hat{z})\,\Re\left[e^{ikx}\left\{ \gamma \mathrm{Ai}\left(e^{i\pi/6}\frac{y}{\delta_s}\right) + \pi Q\,\mathrm{Ai}\left(e^{i\pi/6}\frac{y}{\delta_s}\right)\int_0^{e^{i\pi/6}y/\delta_s} \mathrm{Bi}(s)s\, e^{-s/\Delta_\xi}\, ds + \pi Q\,\mathrm{Bi}\left(e^{i\pi/6}\frac{y}{\delta_s}\right)\int_{e^{i\pi/6}y/\delta_s}^\infty \mathrm{Ai}(s)s\, e^{-s/\Delta_\xi}\, ds \right\}\right]. \tag{B.17}$$

Data availability

Data will be made available on request.

References

[1] P. Ricco, M. Skote, M. Leschziner, A review of turbulent skin-friction drag reduction by near-wall transverse forcing, Prog. Aerosp. Sci. 123 (2021) 100713, http://dx.doi.org/10.1016/j.paerosci.2021.100713.

[2] M. Quadrio, P. Ricco, The laminar generalized Stokes layer and turbulent drag reduction, J. Fluid Mech. 667 (2011) 135–157, http://dx.doi.org/10.1017/s0022112010004398.

[3] K.-S. Choi, J.-R. DeBisschop, B.R. Clayton, Turbulent boundary-layer control by means of spanwise-wall oscillation, AIAA J. 36 (7) (1998) 1157–1163, http://dx.doi.org/10.2514/3.13948.

[4] K.-S. Choi, B.R. Clayton, The mechanism of turbulent drag reduction with wall oscillation, Int. J. Heat Fluid Flow 22 (1) (2001) 1–9, http://dx.doi.org/10.1016/S0142-727X(00)00070-9.

[5] P. Ricco, S. Wu, On the effects of lateral wall oscillations on a turbulent boundary layer, Exp. Therm. Fluid Sci. 29 (1) (2004) 41–52, http://dx.doi.org/10.1016/j.expthermflusci.2004.01.010.

[6] E. Touber, M.A. Leschziner, Near-wall streak modification by spanwise oscillatory wall motion and drag-reduction mechanisms, J. Fluid Mech. 693 (2012) 150–200, http://dx.doi.org/10.1017/jfm.2011.507.

[7] L. Agostini, E. Touber, M.A. Leschziner, Spanwise oscillatory wall motion in channel flow: drag-reduction mechanisms inferred from DNS-predicted phase-wise property variations at $Re_\tau = 1000$, J. Fluid Mech. 743 (2014) 606–635, http://dx.doi.org/10.1017/jfm.2014.40.

[8] L. Agostini, E. Touber, M. Leschziner, The turbulence vorticity as a window to the physics of friction-drag reduction by oscillatory wall motion, Int. J. Heat Fluid Flow 51 (2015) 3–15, http://dx.doi.org/10.1016/j.ijheatfluidflow.2014.08.002.

[9] M. Knoop, R. Deshpande, F.F.J. Schrijer, B.W. van Oudheusden, Response of a turbulent boundary layer to steady, square-wave-type transverse wall-forcing, Phys. Rev. Fluids 10 (6) (2025) 064607, http://dx.doi.org/10.1103/PhysRevFluids.10.064607.

[10] M. Quadrio, P. Ricco, C. Viotti, Streamwise-travelling waves of spanwise wall velocity for turbulent drag reduction, J. Fluid Mech. 627 (2009) 161–178, http://dx.doi.org/10.1017/S0022112009006077.

[11] F. Auteri, A. Baron, M. Belan, G. Campanardi, M. Quadrio, Experimental assessment of drag reduction by traveling waves in a turbulent pipe flow, Phys. Fluids 22 (11) (2010) http://dx.doi.org/10.1063/1.3491203.

[12] D. Gatti, A. Güttler, B. Frohnapfel, C. Tropea, Experimental assessment of spanwise-oscillating dielectric electroactive surfaces for turbulent drag reduction in an air channel flow, Exp. Fluids 56 (2015) 1–15, http://dx.doi.org/10.1007/s00348-015-1983-x.

[13] J. Bird, M. Santer, J. Morrison, Experimental control of turbulent boundary layers with in-plane travelling waves, Flow Turbul. Combust. 100 (2018) 1015–1035, http://dx.doi.org/10.1007/s10494-018-9926-2.

[14] C. Viotti, M. Quadrio, P. Luchini, Streamwise oscillation of spanwise velocity at the wall of a channel for turbulent drag reduction, Phys. Fluids 21 (2009) 115109, http://dx.doi.org/10.1063/1.3266945.

[15] S.P. Wilkinson, Investigation of an oscillating surface plasma for turbulent drag reduction, in: 41st Aerospace Sciences Meeting and Exhibit, 2003, p. 1023, http://dx.doi.org/10.2514/6.2003-1023.

[16] T.C. Corke, F.O. Thomas, Active and passive turbulent boundary-layer drag reduction, AIAA J. 56 (10) (2018) 3835–3847, http://dx.doi.org/10.2514/1.J056949.

[17] F. Thomas, T. Corke, A. Duong, S. Midya, K. Yates, Turbulent drag reduction using pulsed-DC plasma actuation, J. Phys. D: Appl. Phys. 52 (43) (2019) 434001, http://dx.doi.org/10.1088/1361-6463/ab3388.

[18] S.H. Schaafsma, Transverse Forcing by Acoustic Excitation (Master's thesis), Delft University of Technology, Delft, The Netherlands, 2025, URL: https://resolver.tudelft.nl/uuid:554fdd0c-ef09-4156-8fa9-756523fd8f7f.

[19] T.W. Berger, J. Kim, C. Lee, J. Lim, Turbulent boundary layer control utilizing the Lorentz force, Phys. Fluids 12 (3) (2000) 631–649, http://dx.doi.org/10.1063/1.870270.

[20] C. Lee, J. Kim, Control of the viscous sublayer for drag reduction, Phys. Fluids 14 (7) (2002) 2523–2529, http://dx.doi.org/10.1063/1.1454997.

[21] K.S. Breuer, J. Park, C. Henoch, Actuation and control of a turbulent channel flow using Lorentz forces, Phys. Fluids 16 (4) (2004) 897–907, http://dx.doi.org/10.1063/1.1647142.

[22] S. Chernyshenko, Drag reduction by a solid wall emulating spanwise oscillations. Part 1, 2013, http://dx.doi.org/10.48550/arXiv.1304.4638, arXiv.

[23] S. Ghebali, S. Chernyshenko, M. Leschziner, Can large-scale oblique undulations on a solid wall reduce the turbulent drag? Phys. Fluids 29 (10) (2017) 105102, http://dx.doi.org/10.1063/1.5003617.

[24] H. Lienhart, M. Breuer, C. Köksoy, Drag reduction by dimples?–A complementary experimental/numerical investigation, Int. J. Heat Fluid Flow 29 (3) (2008) 783–791, http://dx.doi.org/10.1016/j.ijheatfluidflow.2008.02.001.

[25] C.M.J. Tay, B.C. Khoo, Y.T. Chew, Mechanics of drag reduction by shallow dimples in channel flow, Phys. Fluids 27 (3) (2015) http://dx.doi.org/10.1063/1.4915069.

[26] M. van Nesselrooij, L. Veldhuis, B. Van Oudheusden, F. Schrijer, Drag reduction by means of dimpled surfaces in turbulent boundary layers, Exp. Fluids 57 (9) (2016) 1–14, http://dx.doi.org/10.1007/s00348-016-2230-9.

[27] O. Van Campenhout, M. Van Nesselrooij, Y. Lin, J. Casacuberta, B. van Oudheusden, S. Hickel, Experimental and numerical investigation into the drag performance of dimpled surfaces in a turbulent boundary layer, Int. J. Heat Fluid Flow 100 (2023) 109110, http://dx.doi.org/10.1016/j.ijheatfluidflow.2023.109110.

[28] M. Van Nesselrooij, O. Van Campenhout, L. Veldhuis, Body provided with a superficial area adapted to reduce drag, 2020, US Patent 10, 851, 817.

[29] Y. Peet, P. Sagaut, Y. Charron, Turbulent drag reduction using sinusoidal riblets with triangular cross-section, in: 38th Fluid Dynamics Conference and Exhibit, 2008, p. 3745, http://dx.doi.org/10.2514/6.2008-3745.

[30] M. Sasamori, H. Mamori, K. Iwamoto, A. Murata, Experimental study on drag-reduction effect due to sinusoidal riblets in turbulent channel flow, Exp. Fluids 55 (10) (2014) 1828, http://dx.doi.org/10.1007/s00348-014-1828-z.

[31] G. Cafiero, G. Iuso, Drag reduction in a turbulent boundary layer with sinusoidal riblets, Exp. Therm. Fluid Sci. 139 (2022) 110723, http://dx.doi.org/10.1016/j.expthermflusci.2022.110723.

[32] G. Cafiero, E. Amico, G. Iuso, Manipulation of a turbulent boundary layer using sinusoidal riblets, J. Fluid Mech. 984 (2024) A59, http://dx.doi.org/10.1017/jfm.2024.256.

[33] J. Kim, F. Hussain, Propagation velocity of perturbations in turbulent channel flow, Phys. Fluids A 5 (3) (1993) 695–706, http://dx.doi.org/10.1063/1.858653.

[34] J. Carrasco Grau, O.W. van Campenhout, F.H. Hartog, M. van Nesselrooij, W.J. Baars, F.F. Schrijer, Experimental investigation into the drag performance of Chevron-shaped protrusions in wall-bounded turbulence, Flow Turbul. Combust. 113 (1) (2024) 159–175, http://dx.doi.org/10.1007/s10494-023-00451-0.

[35] R. Örlü, J.H. Fransson, P.H. Alfredsson, On near wall measurements of wall bounded flows—The necessity of an accurate determination of the wall position, Prog. Aerosp. Sci. 46 (8) (2010) 353–387, http://dx.doi.org/10.1017/S0022112010003113.

[36] K.A. Chauhan, P.A. Monkewitz, H.M. Nagib, Criteria for assessing experiments in zero pressure gradient boundary layers, Fluid Dyn. Res. 41 (2) (2009) 021404, http://dx.doi.org/10.1088/0169-5983/41/2/021404.

[37] F. Scarano, M.L. Riethmuller, Advances in iterative multigrid PIV image processing, Exp. Fluids 29 (Suppl 1) (2000) S051–S060, http://dx.doi.org/10.1007/s003480070007.

[38] F. Scarano, Iterative image deformation methods in PIV, Meas. Sci. Technol. 13 (1) (2002) R1–R19, http://dx.doi.org/10.1088/0957-0233/13/1/201.

[39] A. Sciacchitano, B. Wieneke, PIV uncertainty propagation, Meas. Sci. Technol. 27 (8) (2016) 084006, http://dx.doi.org/10.1088/0957-0233/27/8/084006.

[40] B. Launder, W. Rodi, The turbulent wall jet measurements and modeling, Annu. Rev. Fluid Mech. 15 (1) (1983) 429–459, http://dx.doi.org/10.1146/annurev.fl.15.010183.002241.

[41] S.J. Kline, W.C. Reynolds, F.A. Schraub, P.W. Runstadler, The structure of turbulent boundary layers, J. Fluid Mech. 30 (4) (1967) 741–773, http://dx.doi.org/10.1017/S0022112067001740.

[42] J. Jiménez, A. Pinelli, The autonomous cycle of near-wall turbulence, J. Fluid Mech. 389 (1999) 335–359, http://dx.doi.org/10.1017/S0022112099005066.

[43] J.-I. Choi, C.-X. Xu, H.J. Sung, Drag reduction by spanwise wall oscillation in wall-bounded turbulent flows, AIAA J. 40 (5) (2002) 842–850, http://dx.doi.org/10.2514/2.1750.

[44] M. Quadrio, P. Ricco, Critical assessment of turbulent drag reduction through spanwise wall oscillations, J. Fluid Mech. 521 (2004) 251–271, http://dx.doi.org/10.1017/S0022112004001855.

[45] A. Yakeno, Y. Hasegawa, N. Kasagi, Modification of quasi-streamwise vortical structure in a drag-reduced turbulent channel flow with spanwise wall oscillation, Phys. Fluids 26 (8) (2014) 085109, http://dx.doi.org/10.1063/1.085109.

[46] L. Ding, L.F. Sabidussi, B.C. Holloway, M. Hultmark, A.J. Smits, Acceleration is the key to drag reduction in turbulent flow, Proc. Natl. Acad. Sci. 121 (43) (2024) e2403968121, http://dx.doi.org/10.1073/pnas.2403968121.

[47] D. Gatti, M. Quadrio, Reynolds-number dependence of turbulent skin-friction drag reduction induced by spanwise forcing, J. Fluid Mech. 802 (2016) 553–582, http://dx.doi.org/10.1017/jfm.2016.485.

[48] M.W. Knoop, Spanwise Forcing for Turbulent Drag Reduction (Master's thesis), Delft University of Technology, Delft, The Netherlands, 2023, URL: https://resolver.tudelft.nl/uuid:b60d4b92-da7a-4fdb-bac4-2339f2105bdc.

[49] M. Van Nesselrooij, O. Van Campenhout, B. Van Oudheusden, F. Schrijer, L. Veldhuis, Development of an experimental apparatus for flat plate drag measurements and considerations for such measurements, Meas. Sci. Technol. 33 (5) (2022) 055303, http://dx.doi.org/10.1088/1361-6501/ac527f.

[50] P.M. Morse, H. Feshbach, Methods of Theoretical Physics, Technology Press, 1946.